



BNL-224884-2023-JAAM

GRP-COEE-18

# Anion-tethered Single Lithium-ion Conducting Polyelectrolytes through UV-induced Free Radical Polymerization for Improved Morphological Stability of Lithium Metal Anodes

Y. He, E. Hu

To be published in "Angewandte Chemie International Edition"

September 2023

Chemistry Department  
**Brookhaven National Laboratory**

**U.S. Department of Energy**

USDOE Office of Energy Efficiency and Renewable Energy (EERE), Vehicle Technologies Office  
(EE-3V)

Notice: This manuscript has been authored by employees of Brookhaven Science Associates, LLC under Contract No. DE-SC0012704 with the U.S. Department of Energy. The publisher by accepting the manuscript for publication acknowledges that the United States Government retains a non-exclusive, paid-up, irrevocable, world-wide license to publish or reproduce the published form of this manuscript, or allow others to do so, for United States Government purposes.

## **DISCLAIMER**

This report was prepared as an account of work sponsored by an agency of the United States Government. Neither the United States Government nor any agency thereof, nor any of their employees, nor any of their contractors, subcontractors, or their employees, makes any warranty, express or implied, or assumes any legal liability or responsibility for the accuracy, completeness, or any third party's use or the results of such use of any information, apparatus, product, or process disclosed, or represents that its use would not infringe privately owned rights. Reference herein to any specific commercial product, process, or service by trade name, trademark, manufacturer, or otherwise, does not necessarily constitute or imply its endorsement, recommendation, or favoring by the United States Government or any agency thereof or its contractors or subcontractors. The views and opinions of authors expressed herein do not necessarily state or reflect those of the United States Government or any agency thereof.

# Anion-tethered Single Lithium-ion Conducting Polyelectrolytes through UV-induced Free Radical Polymerization for Improved Morphological Stability of Lithium Metal Anodes

Yubin He, Chunyang Wang, Peichao Zou, Ruoqian Lin, Enyuan Hu, and Huolin L. Xin\*

**Abstract:** Single Li<sup>+</sup> ion conducting polyelectrolytes (SICs), which feature covalently tethered counter-anions along their backbone, have the potential to mitigate dendrite formation by reducing concentration polarization and preventing salt depletion. However, due to their low ionic conductivity and complicated synthetic procedure, the successful validation of these claimed advantages in lithium metal (Li<sup>0</sup>) anode batteries remains limited. In this study, we fabricated a SIC electrolyte using a single-step UV polymerization approach. The resulting electrolyte exhibited a high Li<sup>+</sup> transference number ( $t_+$ ) of 0.85 and demonstrated good Li<sup>+</sup> conductivity ( $6.3 \times 10^{-5}$  S/cm at room temperature), which is comparable to that of a benchmark dual ion conductor (DIC,  $9.1 \times 10^{-5}$  S/cm). Benefitting from the high transference number of SIC, it displayed a three-fold higher critical current density ( $2.4 \text{ mA/cm}^2$ ) compared to DIC ( $0.8 \text{ mA/cm}^2$ ) by successfully suppressing concentration polarization-induced short-circuiting. Additionally, the  $t_+$  significantly influenced the deposition behavior of Li<sup>0</sup>, with SIC yielding a uniform, compact, and mosaic-like morphology, while the low  $t_+$  DIC resulted in a porous morphology with Li<sup>0</sup> whiskers. Using the SIC electrolyte, Li<sup>0</sup>||LiFePO<sub>4</sub> cells exhibited stable operation for 4500 cycles with 70.5% capacity retention at 22°C.

## Introduction

Lithium metal (Li<sup>0</sup>) batteries have gained recognition for their exceptional energy density, primarily attributed to the high specific capacity of the lithium metal (Li<sup>0</sup>) anode (3860 mAh/g).<sup>[1]</sup> However, implementing this promising technology using conventional liquid-state electrolytes, typically consist of flammable organic solvents and dissolved lithium salts, has proven challenging. The near-zero mechan-

ical modulus of liquid electrolytes is known to facilitate the formation of Li<sup>0</sup> whisker during charging, which can penetrate the separator and cause battery short-circuits.<sup>[2]</sup> Safety concerns arise from the lithium salts in liquid electrolytes, including Al current collector corrosion with LiTFSI,<sup>[3]</sup> HF generation and low thermal stability associated with LiPF<sub>6</sub>,<sup>[4]</sup> and the explosive nature of LiClO<sub>4</sub>.<sup>[5]</sup> Additionally, the mobility of anions in the electrolyte contributes to the issue of a low Li<sup>+</sup> transference number ( $t_+$ ), wherein the redox Li<sup>+</sup> moves toward the working electrode while the counter ion carrying the opposite charge moves in the opposite direction and accumulates at the counter electrode.<sup>[6]</sup> This process causes concentrate polarization and salt depletion, which drive whisker formation, promote side reactions, and impact the cell's output energy.<sup>[7]</sup>

Polyelectrolytes, in contrast to liquid electrolytes or polymer electrolytes, are macromolecules that contain ionizable groups along their backbones. These ionizable groups dissociate into charged species (mobile Li<sup>+</sup> and immobilized anions) facilitated by ion-solvating moieties.<sup>[8]</sup> The Li<sup>+</sup> ions then coordinate and form complexes with ion-solvating moieties like ethylene oxide moieties (EO). The breaking and formation of lithium-oxygen (Li-O) bonds promote ion transport through the polyelectrolyte.<sup>[9]</sup> As the ligands for Li<sup>+</sup> solvation are gradually replaced, continuous segmental rearrangement allows for the long-range displacement of lithium ions.<sup>[10]</sup> Anchored anions, through their covalent bonding with the polymer matrix, enable the Li<sup>+</sup> ion to become the sole charge carrier in the system, significantly mitigating the low  $t_+$  issue and safety concerns mentioned above.<sup>[11]</sup> Compared to ceramic/inorganic electrolytes, which also exhibits close to unity  $t_+$ , polyelectrolytes offer improved interface stability, processability, and enhanced electrochemical stability due to the high flexibility of polymer chains and compatibility with conventional solid electrolyte interface (SEI) forming additives. However, their main drawback is the low ionic conductivity caused by insufficient ion dissociation and slow chain relaxation, which hinder the conduction of Li<sup>+</sup> ions.<sup>[12]</sup>

The dissociation energy barrier for ion pairs can be reduced by designing anions with conjugated structures to facilitate the delocalization of their negative charge.<sup>[13]</sup> For example, bis-(trifluoromethylsulfonyl) imide (TFSI<sup>-</sup>) has been reported to exhibit weaker pairing strength with Li<sup>+</sup>, leading to improved dissociation compared to conventional anions such as -COO<sup>-</sup>, SO<sub>4</sub><sup>2-</sup>, PO<sub>4</sub><sup>3-</sup>.<sup>[14]</sup> Further enhancement in conductivity can be achieved by replacing

the =O moieties with stronger electro-withdrawing groups.<sup>[12c]</sup> However, this approach involves a complex synthetic procedure. Another viable strategy for improving conductivity is the construction of a block copolymer architecture.<sup>[15]</sup> In this architecture, the soft blocks are densely grafted with ionizable groups and ion-solvating moieties to facilitate Li<sup>+</sup> conduction, while the rigid neutral block provides mechanical reinforcement.<sup>[16]</sup> The self-assembly of these block copolymers into a bi-continuous, phase-separated morphology effectively reduces the tortuosity of ion conduction pathways, enabling good ion-transport properties while maintaining mechanical robustness. Despite steady improvements achieved thus far, polyelectrolyte single ion conductors (SICs) still exhibit moderate ion conductivity, typically on the order of 10<sup>-7</sup> S/cm, which is substantially lower than the target of 10<sup>-4</sup> S/cm proposed by Goodenough.<sup>[17]</sup> Due to limitations in conductivity and challenging synthesis, the anticipated benefits of SICs, such as minimized concentration polarization, inhibited Li<sup>0</sup> whisker formation, and improved full cell durability, are seldom successfully demonstrated in practical lithium metal batteries.

Herein, by utilizing a solvent-free, UV-induced free-radical polymerization platform, we achieved the one-pot production of SIC electrolyte from a precursor solution comprising ionizable monomer, crosslinker, and oligomeric polyethylene oxide plasticizer (PEG<sub>250</sub>) (Figure 1a). The addition of PEG<sub>250</sub> plasticizer effectively promoted chain segmental motion, as evidenced by a significant decrease in the glass transition temperature (T<sub>g</sub>) from 8.3 to -77.2 °C. This accelerated chain relaxation reduced the energy barrier and activation energy for ion conduction, resulting in a good ionic conductivity of 7.4 × 10<sup>-5</sup> S/cm at 30 °C and 1.9 × 10<sup>-4</sup> S/cm at 60 °C. Moreover, the synthesized SIC membrane

exhibited a t<sub>+</sub> of 0.85, which is two-fold higher than the benchmark DIC electrolyte (0.39) with the same polymer chemistry but different anion configurations (covalently tethered vs free mobile, Figure 1b, 1c). The high t<sub>+</sub> and homogeneous distribution of anions in SIC enabled an improved critical current density of 2.4 mA/cm<sup>2</sup>. In contrast, the baseline DIC experienced soft-shortening at 0.8 mA/cm<sup>2</sup> due to severe concentration polarization and salt depletion near the electrode. Through in situ optical microscopy, we observed that the high t<sub>+</sub> of SIC also facilitated the formation of a smooth and dense morphology for plated Li<sup>0</sup>. Cryogenic transmission electron microscopy (Cryo-TEM) further revealed a non-dendritic nano-morphology of Li<sup>0</sup> deposition, with uniformly packed Li<sup>0</sup> domes that were intimately protected by a compact SEI layer. Due to this high t<sub>+</sub> and improved morphological stability of Li<sup>0</sup>, Li<sup>0</sup> || LiFePO<sub>4</sub> full cells utilizing SIC demonstrated good durability of 4500 cycles with a high capacity retention of 70.5 %, at 0.5 C and room temperature.

## Results and Discussion

SIC electrolytes typically exhibit ion conductivity that is 2–3 orders of magnitude lower than DICs, mainly due to the low dissociation of ion pairs<sup>[12c]</sup> and the sluggish relaxation of polymer segments.<sup>[12b]</sup> To address this issue, the introduction of inorganic or organic plasticizers,<sup>[18]</sup> such as TiO<sub>2</sub>, Al<sub>2</sub>O<sub>3</sub>,<sup>[19]</sup> succinonitrile,<sup>[20]</sup> and ionic liquids,<sup>[21]</sup> has been proven effective in enhancing polymer chain mobility and promote ion conduction. PEG<sub>250</sub>, a short-chain oligomer of polyethylene oxide (PEO), possesses excellent solvating ability towards lithium salt, and lower volatility and flammability compared to conventional liquid electrolytes.<sup>[22]</sup> Considering

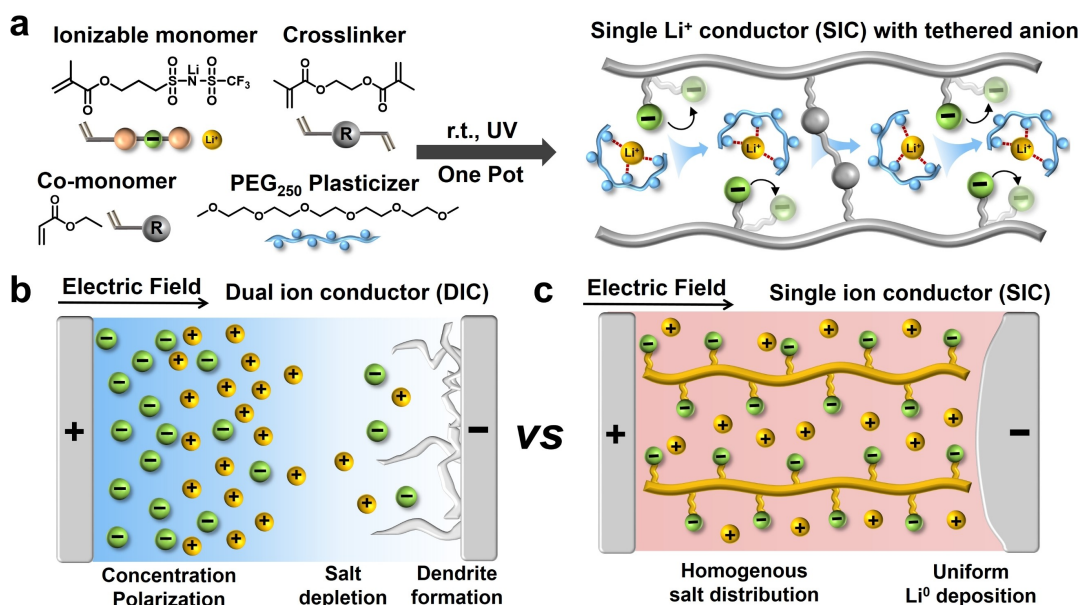


**Figure 1.** Designing concepts. (a) Schematic illustration showing the UV polymerization approach for synthesizing the SIC electrolytes. (b) Conventional DIC electrolyte leads to dendrite formation issues due to concentration polarization and salt depletion. (c) SIC electrolyte improves Li<sup>0</sup> anode morphological stability due to the homogeneous distribution of tethered anions and high t<sub>+</sub>.

the well-documented relationship between molecular weight and segmental mobility, where decreasing molecular weight results in decreased chain entanglement and increased molecular mobility,<sup>[23]</sup> a lower molecular weight of PEG can more effectively enhance the relaxation of the SIC backbone and contribute to higher conductivity.<sup>[24]</sup> To strike a balance between conductivity and thermal stability, a molecular weight of 250 Da was chosen for PEG. This molecular weight ensures sufficient conductivity for investigating the distinct electrochemical behavior between SIC and DIC, while also providing better thermal stability compared to conventional liquid/gel electrolytes which contain flammable solvents such as dimethyl carbonate and 1,3-Dioxolane.

Figure S1 shows that the non-plasticized SIC polymer exhibits a high glass transition temperature ( $T_g$ ) of 8.3 °C. Upon the addition of PEG<sub>250</sub>, a significant decrease in  $T_g$  to -51.8 °C is observed (Figure 2a). Furthermore, increasing the EO:Li molar ratio from 5:1 to 21:1 results in a further decrease in  $T_g$  to -77.2 °C, indicating high polymer segmental mobility that can reduce the energy barrier for ion conduction.<sup>[12b]</sup> As shown in Figure 2b, SIC-3 with an EO:Li ratio of 20.9 exhibits an improved ionic conductivity of  $7.4 \times 10^{-5}$  S/cm at 30 °C and  $1.9 \times 10^{-4}$  S/cm at 60 °C. Moreover, the temperature-dependence of ionic conductivity follows the Vogel-Fulcher-Tammann (VTF) equation instead of the Arrhenius equation (Figure 2c), suggesting the involvement of polymer chain relaxation in the ion conduction process.<sup>[25]</sup> In the VTF equation, the pre-exponential factor  $A$  represents the effective concentration of charge carriers, while the activation energy,  $E_a$ , indicates the energy barrier that  $\text{Li}^+$  must overcome to transport through the electrolyte.<sup>[26]</sup>

With an increasing EO:Li ratio, the activation energy decreased from 9.95 to 7.72 kJ/mol (Figure 2d), attributing to enhanced chain relaxations and lowered  $T_g$ . Consequently, the conductivity increases from  $8.97 \times 10^{-6}$  S/cm for SIC-1 to  $7.44 \times 10^{-5}$  S/cm for SIC-3.

To study the effect of anion configuration on the ion transport kinetics, we also synthesized a DIC electrolyte containing both mobile  $\text{Li}^+$  and mobile anions using the same UV polymerization approach. The  $\text{Li}^+$  concentration, EO:Li ratio, and crosslinking density were controlled to be comparable to those of SIC-3 (Table S1). Figures 2a to 2d show that DIC-1 has a comparable  $T_g$  of -76.5 °C, but exhibits a higher conductivity of  $2.35 \times 10^{-4}$  S/cm at 30 °C. The VTF fitting analysis further revealed a reduction in the activation energy (7.30 kJ/mol) and an increase in the pre-exponential factor  $A$ , which could be explained by the weakened inter-chain interaction due to the absence of tethered ionic groups and improved ion pair dissociation, which enhances the effective concentration of charge carriers. However, despite its higher conductivity, DIC-1 has a  $t_{\text{Li}^+}$  of only 0.39, indicating that 61 % of the electric current is carried by the anions that do not participate in the redox reactions (Figure 2e). This is in sharp contrast to SIC-3, which has a  $t_{\text{Li}^+}$  of 0.85 due to the covalent tethering of anions onto the backbones (Figure 2f). The high  $t_{\text{Li}^+}$  value of SIC-3 suggests a high degree of polymerization of the ionizable monomer. Notably, the NMR characterization presented in Figure S6 demonstrates almost complete conversion of the monomer, indicating nearly quantitative monomer conversion yield. Moreover, the determination of the gel fraction (insoluble fraction)<sup>[27]</sup> as approximately 95 %

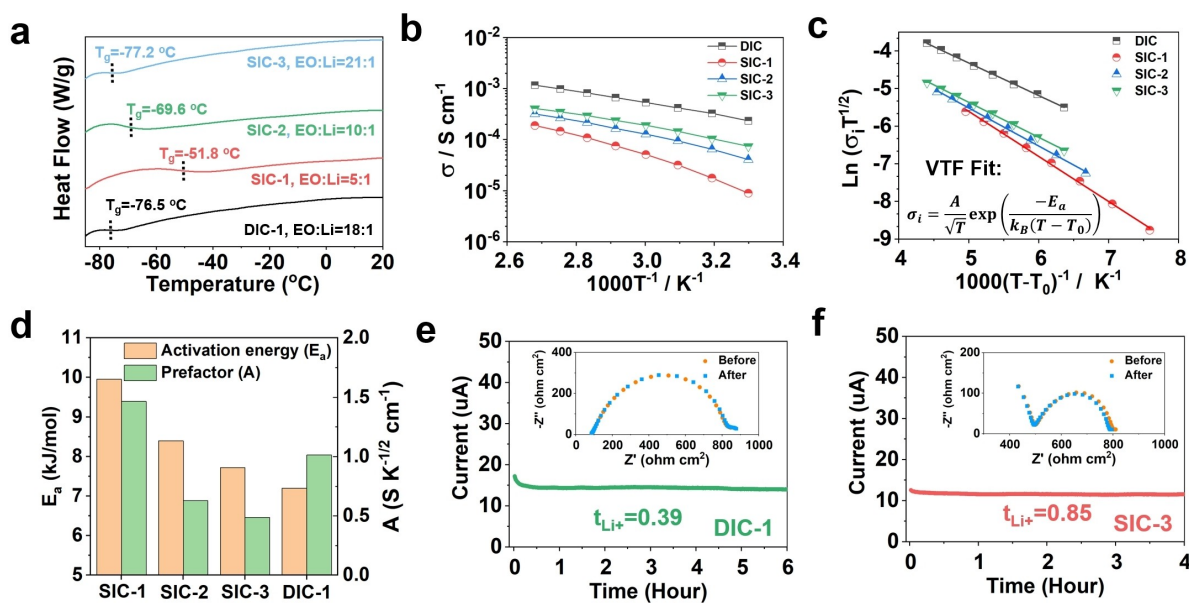


**Figure 2.** Ion transport kinetics of SIC and DIC electrolytes. (a) Glass transition temperatures ( $T_g$ ) of DIC and SIC electrolytes employing different EO:Li molar ratios. (b) Temperature-dependence of ionic conductivities tested by electrochemical impedance spectroscopy (EIS) under cell configuration of SS|electrolyte|SS, where SS refers to stainless steel blocking electrode. (c) VTF fitting results for studying the ion conduction mechanism through the SIC and DIC electrolytes. (d) The activation energy ( $E_a$ ) and pre-exponential factor ( $A$ ) obtained from VTF fitting. (e–f)  $\text{Li}^+$  transference number ( $t_{\text{Li}^+}$ ) of DIC-1 electrolyte (e) and SIC-3 electrolyte (f) measured by the potentialstatic polarization method reported by Bruce and Vincent.<sup>[28]</sup>

(Table S2) further confirms the absence of non-polymerization monomers that could potentially reduce the  $t_+$  value or induce undesired side reactions with the electrode. Overall, this capability of SIC-3 to selectively transport the redox ion while immobilizing the counter-anions is anticipated to play a crucial role in improving the electrochemical performance and regulating the deposition behavior of  $\text{Li}^0$ .

To investigate the impact of  $t_+$  on the electrochemical behavior,  $\text{Li}^0|\text{Li}^0$  symmetric cells were assembled. Subsequently, the critical current density (CCD)<sup>[29]</sup> of the SIC-3 and DIC-1 based cells was evaluated by cycling the cells at incrementally increasing current densities from 0.2 to 3  $\text{mA}/\text{cm}^2$ , while maintaining a fixed charge/discharge time of 1 hour. The SIC-3 electrolyte exhibited a high CCD of 2.4  $\text{mA}/\text{cm}^2$  (Figure 3a). However, the DIC-1 electrolyte, despite its higher conductivity, resulted in cell failure at 0.8  $\text{mA}/\text{cm}^2$  (Figure 3b). Voltage-time curves at different current densities are shown in Figures 3c to 3e. For DIC-1, the cell voltage ramped rapidly from 131 to 221 mV during charging at 0.4  $\text{mA}/\text{cm}^2$ . At higher current densities of 0.8  $\text{mA}/\text{cm}^2$ , an exponential increase in cell voltage was observed, followed by voltage fluctuations indicating micro-shorting within the batteries. This concentration polarization-induced cell failure is commonly observed when operating the battery above the limiting current density. As the current passes through the electrolyte, anions accumulate near the  $\text{Li}^0$  stripping side, while salt depletion occurs near

the  $\text{Li}^0$  plating side.<sup>[30]</sup> Above the limiting current density and with increasing operation time, the salt concentration near the  $\text{Li}^0$  plating side reaches zero, leading to  $\text{Li}^0$  whisker formation and cell failure.<sup>[6,7b]</sup> In contrast, the SIC-3 electrolyte with covalently tethered anions distributed homogeneously within the polymer matrix minimized anion accumulation and salt depletion. From 0.4  $\text{mA}/\text{cm}^2$  to 1.4  $\text{mA}/\text{cm}^2$ , SIC-based cells demonstrated steady and flat voltage profiles with negligible concentration overpotential, indicating an improved limiting current density (1.4  $\text{mA}/\text{cm}^2$  vs 0.4  $\text{mA}/\text{cm}^2$ ) due to its higher  $t_+$ .

Dynamic mechanical analysis results were included to investigate whether the deviation in electrochemical behavior could be attributed to differences in mechanical properties. The measured tensile strengths of DIC-1 and SIC-3 were found to be similar, at 0.25 MPa and 0.26 MPa, respectively (Figure 3f). However, DIC-1 exhibited superior flexibility compared with SIC-3, with a higher elongation at break of 1.5%. The storage modulus for DIC-1 and SIC-3 was determined to be 20 MPa and 60 MPa, respectively, indicating that DIC-1 has a softer nature than SIC-3 (Figure 3g, 3h). The slightly higher storage modulus of SIC-3 may be attributed to the incorporation of ionic groups onto the polymer backbones, which enhances inter-chain interactions. Overall, the mechanical properties of DIC-1 and SIC-3 were found to be similar, given their equivalent crosslinking densities,  $\text{Li}^+$  concentrations, and EO:Li ratios.

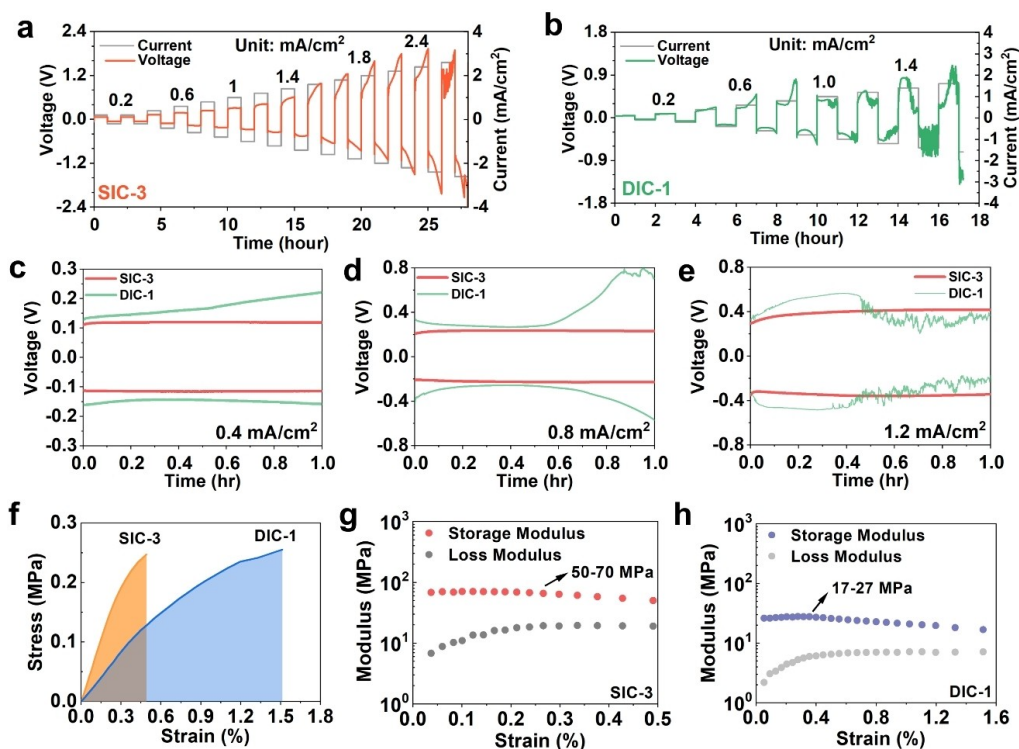


**Figure 3.** Critical current density and mechanical properties. (a–b) Critical current densities of SIC-3 (a) and DIC-1 (b) electrolytes tested at 50 °C, with step-up current densities from 0.2–3  $\text{mA}/\text{cm}^2$ , and fixed charge/discharge time of 1 hour. (c–e) Voltage-time profiles of  $\text{Li}^0|\text{SIC-3}|\text{Li}^0$  and  $\text{Li}^0|\text{DIC-1}|\text{Li}^0$  cells at different current densities of 0.4  $\text{mA}/\text{cm}^2$  (c), 0.8  $\text{mA}/\text{cm}^2$  (d), and 1.2  $\text{mA}/\text{cm}^2$  (e). (f) Tensile strength and elongation at break of SIC-3 and DIC-1 electrolytes measured by dynamic mechanical analysis at r.t. (g–h) Storage modulus and loss modulus of SIC-3 (g) and DIC-1 (h).

Since stable voltage profiles were observed for SIC-based cells, it suggests that electrode-electrolyte delamination did not contribute to the cell failure observed in the DIC-based cell. Moreover, the MPa-level modulus of SIC-3, when compared to conventional liquid electrolytes, may also help regulate the deposition behavior of mossy  $\text{Li}^0$ .<sup>[31]</sup> Additionally, thermal gravimetric analysis (TGA) demonstrated a mass loss of  $<3.7\%$  before  $100^\circ\text{C}$  (Figure S2), offering improved safety compared to flammable and volatile liquid electrolytes.

In addition to a high critical current density of  $2.4\text{ mA/cm}^2$ , the SIC-3 electrolyte also enables stable  $\text{Li}^0$  plating up to a high area capacity of  $3.6\text{ mAh/cm}^2$  (Figure 4a). When charging at a constant current density of  $0.2\text{ mA/cm}^2$  for 18 hours, the  $\text{Li}^0|\text{SIC-3}|\text{Li}^0$  cell exhibits a stable and constant overpotential, with no noticeable concentration polarization observed due to the high  $t_+$  of SIC-3 electrolyte. The intervals indicated by black arrows correspond to pausing the cell operation for electrochemical impedance spectroscopy (EIS) measurements. Consistent with the voltage-capacity profile, the EIS curves show no significant changes in bulk resistance or charge transfer resistance (Figure 4b), indicating the absence of whisker penetration or electrode-electrolyte delamination occurred. On the other hand, the  $\text{Li}^0|\text{DIC-1}|\text{Li}^0$  cell experiences an apparent voltage increase during the first 3 hours, which can be attributed to concentration polarization caused by anion

migration. Furthermore, the EIS profiles measured at 4 hours and 0 hours remain constant (Figure 4c), excluding the possibility that the observed voltage increase was due to electrode-electrolyte delamination or side reactions. After 3 hours, a voltage drop from  $240\text{ mV}$  to  $100\text{ mV}$  occurs within 15 hours ( $3\text{ mAh/cm}^2$ ), and EIS measurements show a significant decrease in charge transfer resistance from  $900$  to  $300\text{ ohm}\cdot\text{cm}^2$ . This suggests the development of non-uniform and dendritic  $\text{Li}^0$  morphology, which may cause micro-shorting inside the battery.<sup>[29]</sup>

To validate this assumption and reveal the macroscopic morphology of deposited  $\text{Li}^0$ , in situ optical cells were assembled. Figure 4d and 4e show digital images of the  $\text{Li}^0$  electrode before and after plating at  $0.2\text{ mA/cm}^2$  for 30 hours. Under DIC-1, the deposited  $\text{Li}^0$  appeared loose, non-uniform, and porous. In comparison,  $\text{Li}^0$  plated under SIC-3 exhibited a dense, compact, and non-dendritic morphology, with a shiny appearance indicating minimized side reactions. Figures 4f–4h further present scanning electron microscope (SEM) images that reveal the micro-scale morphology of  $\text{Li}^0$  deposits. SIC-3 enabled a flat, smooth, mosaic-like surface morphology.  $\text{Li}^0$  chunks with a diameter of  $5\text{--}10\text{ }\mu\text{m}$  were intimately connected, and no  $\text{Li}^0$  whiskers or dendrites were observed even at a large field of view up to  $0.4\times 0.3\text{ mm}$  (Figure S3). This morphology may reduce the formation of isolated  $\text{Li}^0$  and suppress side reactions by decreasing the contact area between  $\text{Li}^0$  and electrolyte.<sup>[32]</sup>

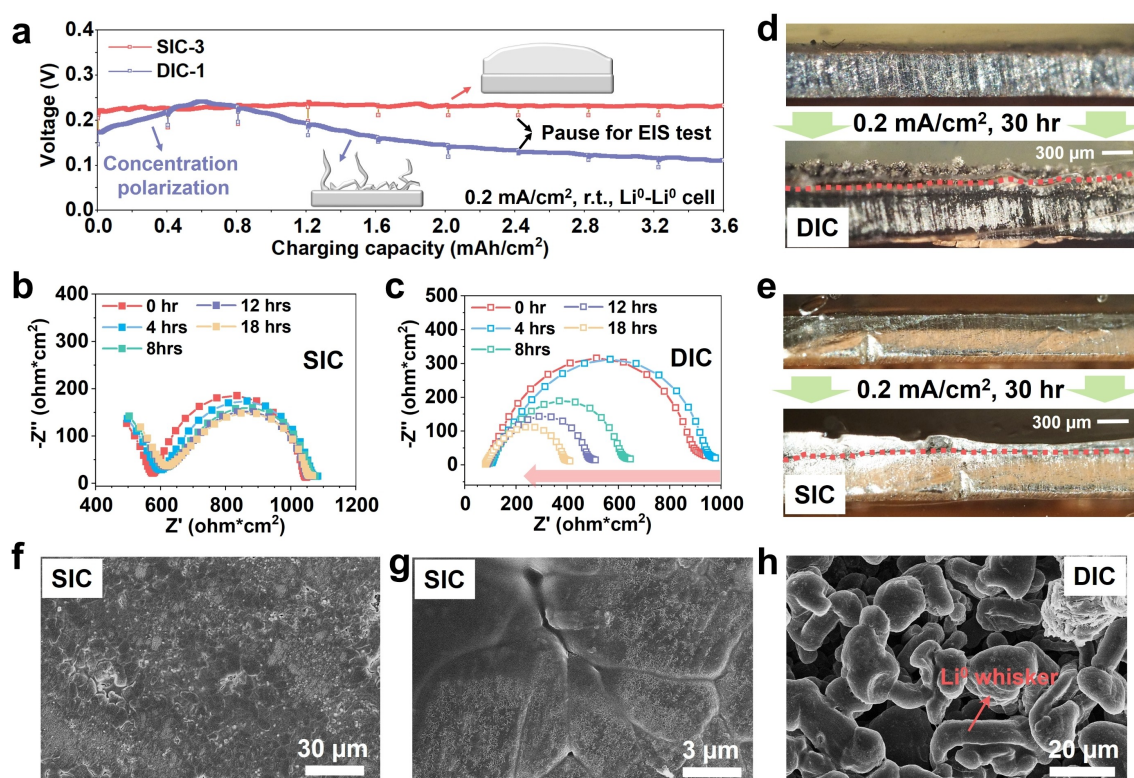


**Figure 4.**  $\text{Li}^0$  plating behavior and morphology. (a) Voltage-capacities profiles when charging the  $\text{Li}^0|\text{SIC-3}|\text{Li}^0$  and  $\text{Li}^0|\text{DIC-1}|\text{Li}^0$  symmetric cells at a constant current density of  $0.2\text{ mA/cm}^2$ . (b–c) Evolution of EIS profiles during the charging process of  $\text{Li}^0/\text{SIC}/\text{Li}^0$  (b) and  $\text{Li}^0|\text{DIC}|\text{Li}^0$  cells (c). (d–e) In situ optical microscope images showing the macroscopic morphology of  $\text{Li}^0$  plated under the DIC-1 (d) and SIC-3 (e) electrolytes. (f–h) SEM characterization showing the surface morphology of plated  $\text{Li}^0$  under the SIC-3 (f,g) and DIC-1 (h) electrolytes.

In contrast, the Li<sup>0</sup> deposits derived from DIC exhibited small whiskers and grains that loosely piled up, resulting in a highly porous and non-uniform morphology consistent with the in situ optical cell characterization (Figure 4h and S4). This observed difference in Li<sup>0</sup> morphology further explains their distinct electrochemical behavior. The low  $t_+$  of DIC contributes to concentration polarization and salt depletion, resulting in the formation of Li<sup>0</sup> whiskers.<sup>[6,33]</sup> The penetration of these Li<sup>0</sup> whiskers into the electrolyte leads to a lower critical current density compared to SIC (0.8 vs 2.4 mA/cm<sup>2</sup>, Figure 3a, 3b). Additionally, the loose and porous morphology of Li<sup>0</sup> increases the contact area between the Li<sup>0</sup> anode and DIC-1, explaining the decrease in charge transfer resistance as depicted in Figure 4c.

To affirm the capability of the SIC-3 electrolyte in facilitating dendrite-free Li<sup>0</sup> deposition, multiscale cryogenic transmission electron microscopy (Cryo-TEM) characterization was employed to investigate the morphological and atomic structure of the deposited Li<sup>0</sup> (refer to the experimental section for detailed methodology). Cryo-TEM images of the deposited Li<sup>0</sup>, as shown in Figures 5a–5c, reveal a uniformly packed morphology with dome-shaped Li<sup>0</sup> crystals, confirming the absence of dendritic structures and aligning with the ex situ SEM results (Figure 4f, 4g). Figure 5d presents a representative electron diffraction pattern (EDP) of the deposited Li<sup>0</sup>, where the Bragg spots correspond to body-centered cubic Li metal. Atomic-reso-

lution Cryo-TEM image (Figure 5e) and the corresponding fast Fourier transform (FFT) (Figure 5f) of the Li<sup>0</sup> deposit demonstrate the formation of an SEI composed of nano-sized domains (e.g., Li<sub>2</sub>O as indicated by yellow circles). The absence of dendritic structures during Li<sup>0</sup> deposition and the uniform morphology of Li<sup>0</sup> deposits, as revealed by Cryo-TEM, provide further support for the enhanced electrochemical properties of the SIC electrolyte. The connection between these microscopic characteristics and the good durability of the Li<sup>0</sup> anode batteries will be further discussed in the subsequent section.

The long-term cycling stability of Li<sup>0</sup>|SIC-3|Li<sup>0</sup> cell was demonstrated in Figure 6a. The cell maintained a constant overpotential of 100 mV and operated stably for 1000 hours at 0.2 mA/cm<sup>2</sup> and 0.2 mAh/cm<sup>2</sup>. Figure 6b shows the extracted voltage-time curves at 2, 500, and 1000 hours, respectively. The low concentration overpotential can be attributed to the high  $t_+$  of SiC-3, which minimized anion accumulation and salt depletion. The overlapping voltage-time curves during cycling indicate a stable interface without dendrite penetration or side reactions between electrode and electrolyte. No fluctuation or a sudden drop in cell voltage was observed, indicating the absence of soft-shortening or hard-shortening during cycling. To further demonstrate electrochemical stability, cycling voltammetry (CV) was performed at a scanning rate of 1 mV/s (Figure 6c). After the first scanning cycle, which allowed for the formation of a

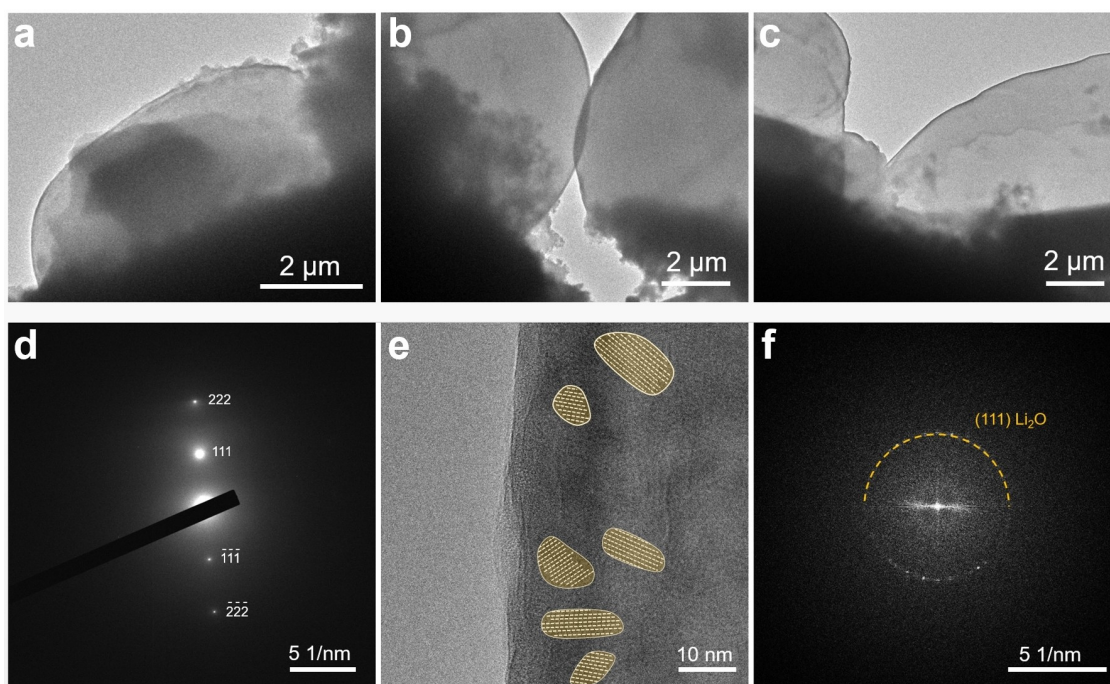


**Figure 5.** Cryo-TEM characterization. (a–c) Representative cryogenic transmission electron microscopy (Cryo-TEM) images reveal the uniform dome-shaped morphology of the Li<sup>0</sup> deposits with SIC electrolyte. (d) A representative electron diffraction pattern (EDP) of a deposited Li<sup>0</sup> crystal, which can be perfectly assigned to body-centered cubic Li metal. (e) A representative atomic-resolution Cryo-TEM image showing the atomic structure of the deposited Li<sup>0</sup>. The Li<sup>0</sup> deposit shows a well-formed SEI composed of nano-sized domains (e.g., Li<sub>2</sub>O as indicated by yellow circles). (f) The fast Fourier transform (FFT) corresponding to the atomic-resolution Cryo-TEM image in (e). A diffraction ring corresponding to the (111) crystallographic planes of polycrystalline Li<sub>2</sub>O is identified (Bragg spots corresponding to other components are not effectively identified due to the large thickness of the Li deposit).

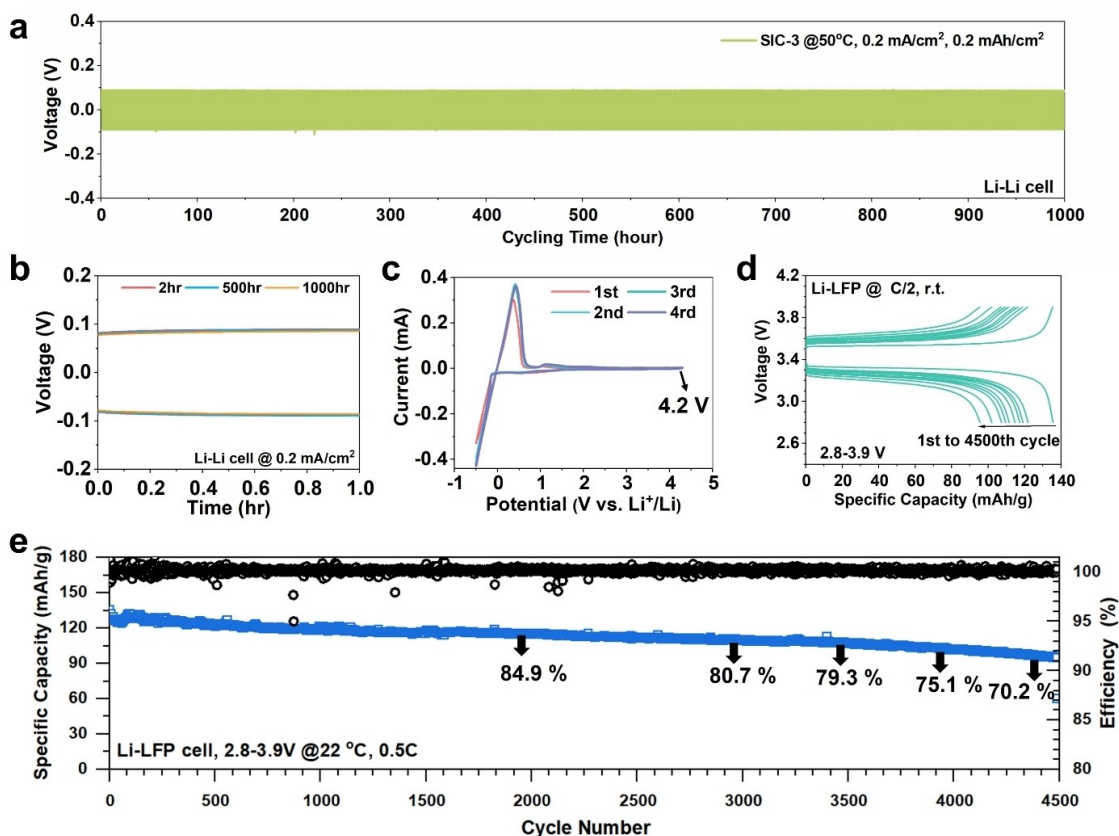


**Figure 6.** Practicability in Li<sup>0</sup> anode batteries. (a) Cycling stability of Li<sup>0</sup>|SIC-3|Li<sup>0</sup> cell when tested at 0.2 mA/cm<sup>2</sup>, 0.2 mAh/cm<sup>2</sup>, and 50°C. (b) Extracted voltage-time curves at 2 hours, 500 hours, and 1000 hours during Li<sup>0</sup>|SIC|Li<sup>0</sup> cell operation. (c) CV profiles of SIC-3 electrolyte measured under Li<sup>0</sup>|SIC|SS configuration with a scanning rate of 1 mV/s, and at r.t. (d) Selected voltage-capacity curves at every 500 cycles during the operation of Li<sup>0</sup>|SIC|LiFePO<sub>4</sub> cell. (e) Long-term cycling performance of Li<sup>0</sup>|SIC|LiFePO<sub>4</sub> cell tested at r.t. and C/2. The loading of active material on the cathode is ≈ 2 mg/cm<sup>2</sup>.

solid electrolyte interface (SEI) layer on the electrode, the Li<sup>0</sup> plating peak (reduction) and Li<sup>0</sup> stripping peak (oxidation) almost overlapped during the 2<sup>nd</sup> to 4<sup>th</sup> cycles, confirming the stable interfacial chemistry between SIC-3 and Li<sup>0</sup>. Additionally, at high voltage ranges, the cell exhibited negligible oxidative current during the positive sweep up to 4.2 V vs Li<sup>+</sup>/Li. This wide electrochemical stability window may be attributed to the absence of terminal hydroxyl groups (–OH) commonly found in conventional PEO-based electrolytes.<sup>[34]</sup>

In Figure 6d, 6e, Li<sup>0</sup> anode full cells with LiFePO<sub>4</sub> as the cathode were assembled, due to its high safety, low cost, and superior stability.<sup>[35]</sup> At room temperature and 0.5 C, the cell demonstrated good durability > 4500 cycles with a capacity retention of 70.5%. The cell capacity at the 1<sup>st</sup>, 1000<sup>th</sup>, 2000<sup>th</sup>, 3000<sup>th</sup>, and 4000<sup>th</sup> cycles were 135.5 mAh/g, 120.5 mAh/g (89%), 115 mAh/g (85%), 109 mAh/g (81%), and 102 mAh/g (75%), respectively. Figure 6d depicts the voltage-capacity curves during cycling, revealing voltage plateaus of 3.53 V during charging and 3.34 V during discharging. After 12,000 hours of operation, the overpotential gradually increased from 195 mV to 401 mV, which is considered the primary reason for capacity fading. Notably, no signs of micro-shorting were observed, confirming the

ability of the SIC electrolyte to maintain stable interfacial chemistry and regulate Li<sup>0</sup> deposition behavior. The good durability of the SIC-3 electrolyte can be attributed to its sufficient Li<sup>+</sup> conductivity ( $6.3 \times 10^{-5}$  S/cm) and an appropriate modulus that strikes a balance between preventing dendrite formation and avoiding electrolyte electrode delamination. Additionally, the stable interfacial chemistry, facilitated by the high  $t_+$  value, the good Li<sup>0</sup> stability of PEG<sub>250</sub>, the solvent-free UV polymerization synthesis, and the SEI forming ability of the FEC additive, further contribute to its overall durability.

To further demonstrate the practicality of this single-ion chemistry, we fabricated a 20- $\mu$ m thick SIC electrolyte using the conventional Celgard<sup>®</sup> separator as a mechanical reinforcement (Figure S5a). Li<sup>0</sup>-Li<sup>0</sup> symmetric cell tests showed stable cycling for ≈ 600 hours at 0.2 mA/cm<sup>2</sup> and 0.2 mAh/cm<sup>2</sup> (Figure S5b). Considering the potential impact of porosity, pore size, or surface chemistry of different reinforcement materials on Li<sup>+</sup> transference, we conducted additional measurements to determine the  $t_+$  value of the SIC-3@Celgard electrolyte. Figure S5c depicts the obtained  $t_+$  value of 0.83, which closely aligns with the value measured using SIC-3@glass fiber. Moreover, the SIC@Celgard electrolyte demonstrates a high tensile strength of

15.6 MPa (Figure S5d) and a storage modulus within the range of 300–600 MPa (Figure S5e), indicating its potential in practical applications.

## Conclusion

In this study, we have developed a single-ion chemistry that exhibits high  $t_+$  (0.85). We systematically investigated the impact of anion tethering on ion transport kinetics, electrochemical properties, and  $\text{Li}^0$  deposition behavior was systematically studied. Our findings revealed that ion conduction through SIC follows the VTF equation, with the polymer chain relaxation playing a crucial role in determining conductivity. The incorporation of a PEG<sub>250</sub> plasticizer significantly enhanced polymer segmental motion ( $T_g$  of  $-77.2^\circ\text{C}$ ), reduced the activation energy for ion conduction (7.72 kJ/mol), and enabled a desirable  $\text{Li}^+$  ion conductivity comparable to DIC electrolyte ( $6.3$  vs  $9.1 \times 10^{-5}$  S/cm). The SIC electrolyte demonstrated a 3-fold higher critical current density compared to DIC ( $2.4$  vs  $0.8$  mA/cm<sup>2</sup>), due to the absence of concentration polarization and salt depletion. Furthermore, the high  $t_+$  of SIC facilitated a dense, uniform, and whisker-free  $\text{Li}^0$  morphology, as confirmed by macroscopic in situ optical scope, micro-scale SEM, and nano-scale Cryo-TEM characterizations. In contrast,  $\text{Li}^0$  deposited under DIC exhibited a loose, porous morphology with whiskers, which can potentially cause cell short-circuiting. When employed in  $\text{Li}^0|\text{Li}^0$  cells, the SIC electrolyte enabled stable cycling for 1000 hours with negligible concentration polarization, and  $\text{Li}^0|\text{LiFePO}_4$  full cell operated for 4500 cycles at room temperature. Overall, this study provides morphological and electrochemical evidence supporting the advantages of single-ion conducting electrolytes, and highlights the need for equal emphasis on  $t_+$  and conductivity in the development of polymer electrolytes or polyelectrolytes.

## Acknowledgements

The development of solid-state electrolyte and the electrochemical tests are supported by the Assistant Secretary for Energy Efficiency and Renewable Energy, Vehicle Technology Office of the U. S. Department of Energy (DOE) through the Advanced Battery Materials Research Program under contract no. DE-SC0012704 and the startup funding of HLX. The Cryo-TEM characterization was supported by the Office of Basic Energy Sciences of the U.S. Department of Energy, under award no. DE-SC0021204. This work made use of facilities and instrumentation at the UC Irvine Materials Research Institute (IMRI), which is supported in part by the National Science Foundation through the UC Irvine Materials Research Science and Engineering Center (DMR-2011967). This research used resources from the Center for Functional Nanomaterials (CFN), which is a U.S. Department of Energy Office of Science User Facility, at Brookhaven National Laboratory under Contract No. DE-SC0012704. We acknowledge Dr. Suvrajit Sengupta and Dr.

John Kelly at the NMR facility in the UCI Department of Chemistry for performing the liquid-state NMR experiments.

## Conflict of Interest

The authors declare no conflict of interest.

## Data Availability Statement

The data that support the findings of this study are available in the supplementary material of this article.

**Keywords:** Lithium Metal Battery · Polyelectrolyte · Single Li+ Conductor · Transference Number

- [1] D. Lin, Y. Liu, Y. Cui, *Nat. Nanotechnol.* **2017**, *12*, 194–206.
- [2] B. Li, Y. Wang, S. Yang, *Adv. Energy Mater.* **2018**, *8*, 1702296.
- [3] J. Kalhoff, D. Bresser, M. Bolloli, F. Alloin, J. Y. Sanchez, S. Passerini, *ChemSusChem* **2014**, *7*, 2939–2946.
- [4] S. E. Sloop, J. B. Kerr, K. Kinoshita, *J. Power Sources* **2003**, *119–121*, 330–337.
- [5] Y. K. Liu, C. Z. Zhao, J. Du, X. Q. Zhang, A. B. Chen, Q. Zhang, *Small* **2023**, *19*, 2205315.
- [6] H. J. Chang, A. J. Ilott, N. M. Trease, M. Mohammadi, A. Jerschow, C. P. Grey, *J. Am. Chem. Soc.* **2015**, *137*, 15209–15216.
- [7] a) J. Xiao, *Science* **2019**, *366*, 426–427; b) C. Brissot, M. Rosso, J. N. Chazalviel, S. Lascaud, *J. Electrochem. Soc.* **1999**, *146*, 4393–4400.
- [8] K. D. Fong, J. Self, K. M. Diederichsen, B. M. Wood, B. D. McCloskey, K. A. Persson, *ACS Cent. Sci.* **2019**, *5*, 1250–1260.
- [9] T. Dam, S. S. Jena, D. K. Pradhan, *Phys. Chem. Chem. Phys.* **2016**, *18*, 19955–19965.
- [10] Z. Xue, D. He, X. Xie, *J. Mater. Chem. A* **2015**, *3*, 19218–19253.
- [11] a) J. Zhu, Z. Zhang, S. Zhao, A. S. Westover, I. Belharouak, P. F. Cao, *Adv. Energy Mater.* **2021**, *11*, 2003836; b) L. Stolz, S. Hochstadt, S. Roser, M. R. Hansen, M. Winter, J. Kasnatscheew, *ACS Appl. Mater. Interfaces* **2022**, *14*, 11559–11566.
- [12] a) Q. Zhao, S. Stalin, C.-Z. Zhao, L. A. Archer, *Nat. Rev. Mater.* **2020**, *5*, 229–252; b) S. Zhao, Y. Zhang, H. Pham, J.-M. Y. Carrillo, B. G. Sumpter, J. Nanda, N. J. Dudney, T. Saito, A. P. Sokolov, P.-F. Cao, *ACS Appl. Energy Mater.* **2020**, *3*, 12540–12548; c) Q. Ma, H. Zhang, C. Zhou, L. Zheng, P. Cheng, J. Nie, W. Feng, Y. S. Hu, H. Li, X. Huang, L. Chen, M. Armand, Z. Zhou, *Angew. Chem. Int. Ed.* **2016**, *55*, 2521–2525.
- [13] R. Bouchet, S. Maria, R. Meziane, A. Aboulaich, L. Lienafa, J. P. Bonnet, T. N. Phan, D. Bertin, D. Gignes, D. Devaux, R. Denoyel, M. Armand, *Nat. Mater.* **2013**, *12*, 452–457.
- [14] P.-F. Cao, B. Li, G. Yang, S. Zhao, J. Townsend, K. Xing, Z. Qiang, K. D. Vogiatzis, A. P. Sokolov, J. Nanda, T. Saito, *Macromolecules* **2020**, *53*, 3591–3601.
- [15] D. Devaux, L. Liénafa, E. Beaudoin, S. Maria, T. N. T. Phan, D. Gignes, E. Giroud, P. Davidson, R. Bouchet, *Electrochim. Acta* **2018**, *269*, 250–261.
- [16] C. Jangu, A. M. Savage, Z. Zhang, A. R. Schultz, L. A. Madsen, F. L. Beyer, T. E. Long, *Macromolecules* **2015**, *48*, 4520–4528.
- [17] J. B. Goodenough, Y. Kim, *Chem. Mater.* **2010**, *22*, 587–603.

- [18] D. Guo, D. B. Shinde, W. Shin, E. Abou-Hamad, A. H. Emwas, Z. Lai, A. Manthiram, *Adv. Mater.* **2022**, *34*, 2201410.
- [19] F. Croce, G. B. Appetecchi, L. Persi, B. Scrosati, *Nature* **1998**, *394*, 456–458.
- [20] a) M. J. Lee, J. Han, K. Lee, Y. J. Lee, B. G. Kim, K. N. Jung, B. J. Kim, S. W. Lee, *Nature* **2022**, *601*, 217–222; b) P. J. Alarco, Y. Abu-Lebdeh, A. Abouimrane, M. Armand, *Nat. Mater.* **2004**, *3*, 476–481.
- [21] a) M. Liu, S. Zhang, E. R. H. van Eck, C. Wang, S. Ganapathy, M. Wagemaker, *Nat. Nanotechnol.* **2022**, *17*, 959–967; b) Y. Wang, C. J. Zanelotti, X. Wang, R. Kerr, L. Jin, W. H. Kan, T. J. Dingemans, M. Forsyth, L. A. Madsen, *Nat. Mater.* **2021**, *20*, 1255–1263.
- [22] E. Glynos, P. Petropoulou, E. Mygiakis, A. D. Nega, W. Pan, L. Papoutsakis, E. P. Giannelis, G. Sakellariou, S. H. Anastasiadis, *Macromolecules* **2018**, *51*, 2542–2550.
- [23] K. Pielichowski, K. Flejtuch, *Polym. Adv. Technol.* **2002**, *13*, 690–696.
- [24] D. Devaux, R. Bouchet, D. Glé, R. Denoyel, *Solid State Ionics* **2012**, *227*, 119–127.
- [25] T. D. Gadim, A. G. Figueiredo, N. C. Rosero-Navarro, C. Vilela, J. A. Gamelas, A. Barros-Timmons, C. P. Neto, A. J. Silvestre, C. S. Freire, F. M. Figueiredo, *ACS Appl. Mater. Interfaces* **2014**, *6*, 7864–7875.
- [26] a) H. Ohno, M. Yoshizawa, *Solid State Ionics* **2002**, *154–155*, 303–309; b) J. L. Thelen, S. Inceoglu, N. R. Venkatesan, N. G. Mackay, N. P. Balsara, *Macromolecules* **2016**, *49*, 9139–9147.
- [27] S. Wang, M. J. Yaszemski, J. A. Gruetzmacher, L. Lu, *Polymer* **2008**, *49*, 5692–5699.
- [28] J. Evans, C. A. Vincent, P. G. Bruce, *Polymer* **1987**, *28*, 2324–2328.
- [29] Y. Lu, C. Z. Zhao, H. Yuan, X. B. Cheng, J. Q. Huang, Q. Zhang, *Adv. Funct. Mater.* **2021**, *31*, 2009925.
- [30] Z. J. Hoffman, A. S. Ho, S. Chakraborty, N. P. Balsara, *J. Electrochem. Soc.* **2022**, *169*, 043502.
- [31] K. Liu, P. Bai, M. Z. Bazant, C.-A. Wang, J. Li, *J. Mater. Chem. A* **2017**, *5*, 4300–4307.
- [32] R. Weber, M. Genovese, A. J. Louli, S. Hames, C. Martin, I. G. Hill, J. R. Dahn, *Nat. Energy* **2019**, *4*, 683–689.
- [33] P. Bai, J. Li, F. R. Brushett, M. Z. Bazant, *Energy Environ. Sci.* **2016**, *9*, 3221–3229.
- [34] X. Yang, M. Jiang, X. Gao, D. Bao, Q. Sun, N. Holmes, H. Duan, S. Mukherjee, K. Adair, C. Zhao, J. Liang, W. Li, J. Li, Y. Liu, H. Huang, L. Zhang, S. Lu, Q. Lu, R. Li, C. V. Singh, X. Sun, *Energy Environ. Sci.* **2020**, *13*, 1318–1325.
- [35] W.-J. Zhang, *J. Power Sources* **2011**, *196*, 2962–2970.
-